ELSEVIER

Contents lists available at ScienceDirect

International Journal of Heat and Mass Transfer

journal homepage: www.elsevier.com/locate/ijhmt



Heat transfer to bouncing droplets on superhydrophobic surfaces



Chunfang Guo a,b, Daniel Maynes b,*, Julie Crockett b, Danyang Zhao a

a Key Laboratory for Precision & Non-traditional Machining Technology of Ministry of Education, Dalian University of Technology, Dalian 116024, China

ARTICLE INFO

Article history: Received 15 October 2018 Received in revised form 9 February 2019 Accepted 17 March 2019

Keywords: Heat transfer Superhydrophobic surfaces Droplet impact Contact time

ABSTRACT

This study experimentally and theoretically investigates the dynamics and heat transfer to impinging water droplets on superhydrophobic surfaces heated below the boiling temperature. Different from impingement on hydrophilic substrates, the droplets rebound from the surface after the spreading and retraction stages. Experiments are performed using simultaneous high speed video and infrared (IR) imaging to capture droplet dynamics and temperature variation during the transient event. Thermal images allow estimation of bulk droplet temperature change during contact such that the cooling effectiveness for an individual droplet can be estimated. A similarity solution is utilized to yield a model for the transient heat flux at the droplet-wall interface, where convection inside the droplet is accounted for. The experimental and theoretical results for the cooling effectiveness show good agreement. It is revealed that the cooling effectiveness increases with Weber number but decreases with droplet diameter and surface cavity fraction (the ratio of cavity area to total surface area).

© 2019 Elsevier Ltd. All rights reserved.

1. Introduction

Heat transfer to impinging liquid droplets is of importance in nature and industrial applications such as spray cooling, fuel injection and inkjet printing [1-3]. In 1966, Wachters et al. [4] studied the heat transfer from a very hot plate to impinging droplets with a sensitive heat flow meter. At surface temperatures above 400 °C, the Leidenfrost boiling state was found to occur, where the heat transfer to the droplet is rather poor. With the development of high speed photography, researchers have a better understanding of droplet impingement. Bernardin et al. [5] used a high speed camera to record the impact behavior of water droplets on a hot aluminum surface and estimated the heat exchange using a thermocouple bonded to the disk underside. A droplet impact and boiling regime map was constructed, which provided a foundation for the research of droplet impingement and associated heat transfer. Experimental studies have explored droplet dynamics and heat transfer for single phase [6], nucleate boiling [7], transition boiling [8] and film boiling scenarios [9].

Pasandideh-Fard et al. [10] considered the impact of water droplets on a hot stainless steel surface through experiments and a Volume-of-Fluid(VOF) model. They proposed a quantitative measure of droplet cooling, cooling effectiveness, relating the actual heat transfer to the maximum possible heat transfer. A simple

* Corresponding author.

E-mail address: maynes@byu.edu (D. Maynes).

model was also developed to estimate the heat transfer during droplet spreading by one-dimensional conduction across a boundary layer. Strotos et al. [11] studied fluid flow and heat transfer during droplet impingement. Using a VOF methodology they proposed an expression to model the cooling effectiveness of an impacting droplet based on the exact analytical solution of two contacting semi-infinite media. Roisman [12] evaluated a similarity solution for a spreading liquid film on a substrate which included mass, momentum and energy to capture the flow and heat transfer of the system. This solution was later applied to model the heat transfer to impinging droplets and compared with experiments, showing good agreement [7,13–15].

In recent years, high speed infrared (IR) thermography has emerged as an effective, non-intrusive method to measure surface temperature. Experimental measurements using thermography yield significantly better spatial resolution and higher response time compared with thermocouples embedded in a substrate. IR imaging was employed to quantify the transient contact temperature during dropwise cooling on infrared-transparent substrates [16]. Combining high-speed video and IR imaging, Shen et al. [17] examined the hydrodynamics and near surface temperature characteristics of water droplets impinging on smooth and nanostructured surfaces. Dissipated energy during impact decreased and evaporative cooling increased on the nano-structured surface relative to smooth. Dunand et al. [18] measured the temperature change of the rear face of a nickel sample using an IR camera to estimate the wall heat flux during Leidenfrost droplet impact using

^b Department of Mechanical Engineering, Brigham Young University, UT 84602, USA

Nomenclature α thermal diffusivity D_0 initial droplet diameter spreading ratio thermal effusivity $\beta_{"}$ q(t)heat flux cavity fraction cooling effectiveness k thermal conductivity ϵ liquid surface tension Q heat transfer normalized time radial coordinate density time 'n initial condition contact time $t_{\rm contact}$ air air property maximum spreading time $t_{ m max}$ d0 initial droplet condition oscillation period $t_{\rm osc}$ df final droplet condition U uncertainty droplet region и velocity interface solid-liquid interface initial droplet velocity v_0 maximum spreading condition We Weber number max radial component vertical coordinate sil silicon property similarity variable $\dot{\nabla}$ initial wall condition wΩ Laplace operator w wall region θ_0 contact angle on the smooth surface vertical component Cassie-Baxter contact angle θ_{CB} A(t)contact area $E_{\mathbf{k}}$ initial kinetic energy specific heat capacity E_{s} surface energy $\vec{D}(t)$ droplet diameter

an inverse heat conduction model. They proposed that the heat removed by evaporation is dominant for smaller droplets and that heat transfer increases with increasing Weber number. Heat transfer to bouncing droplets in the film boiling regime, where surface wettability is less important, was similarly characterized by IR imaging, and the heat transfer coefficient was found to be only weakly dependent on the Weber number [19]. Chatzikyriakou et al. [20] calculated the local heat flux during droplet impingement by measuring the droplet/wall interface temperature on an IR-transparent wafer. Jung et al. [21] investigated the heat transfer characteristics of impinging droplets on an IR-transparent heated surface maintained at temperatures ranging from 176 to 375 °C. Temporally and spatially resolved heat flux was obtained from the thermal images and further used to detect the dynamic Leidenfrost point.

Hydrophobic surfaces that are fabricated with micro/nano structures become superhydrophobic (SH), with contact angles greater than 120°. When liquid is in contact with a SH surface, provided the Cassie (non-wetting) state is maintained, it contacts only the top of the micro- or nanostructures, with a large fraction of the liquid in contact with trapped air in the cavity regions. When a droplet impacts a SH surface complete rebound is usually achieved due to a reduction in viscous losses at the underlying air pockets [22,23]. Thus surface cavity fraction, defined as the ratio of the projected cavity area to the total surface area, plays an important role in droplet/wall interactions [24]. Prior research has explored heat transfer dynamics of droplets on SH surfaces, including dropwise condensation [25,26], ice formation [27,28], droplet atomization [29,30] and droplet evaporation [31,32]. It was demonstrated that evaporation times of sessile droplets on SH surfaces increase with substrate cavity fraction while overall heat transfer rates decrease [31]. Other studies have shown reductions in heat transfer for liquid flow through SH channels [33] and for jet impingement on SH surfaces [34].

For droplet impingement on SH surfaces, shorter contact time and reduced solid-liquid contact significantly alter the net heat transfer. Rosengarten et al. [35] presented a preliminary investigation into the effect of superhydrophobicity on the heat transfer to impinging droplets using IR thermography and found that the

overall cooling effect of impacting droplets is significantly reduced on SH surfaces relative to hydrophilic surfaces. Shiri et al. [36] used an IR camera to measure the surface temperature on a SH surface after droplet detachment and performed scale analyses using a simplified heat conduction model. They demonstrated that the heat exchange between droplets and SH surfaces is much less than on hydrophilic surfaces.

Previous measurements of heat transfer to impinging droplets have generally used the temperature change of the impinged substrate to infer the total energy change of the drop during the impingement event. In this study, the bulk temperature change of droplets over the course of the impingement event is directly measured by IR imaging and is used to calculate the overall cooling effectiveness. Further, we extend a previously verified theoretical heat transfer model to account for the differing thermal and flow dynamics on SH surfaces. Cavity fraction has an important effect on droplet impact dynamics and the corresponding heat transfer, which has not been quantified. Specifically, the influence of surface cavity fraction, impact Weber number, and droplet size is revealed in the experimental and model results. Experimental measurements of overall heat transfer to bouncing droplets is compared with theoretical results and good agreement is obtained.

2. Experimental methodology

2.1. Surface fabrication

SH surfaces used for the experiments were fabricated on polished silicon wafers with 500 μ m thickness and 100 mm diameter. Micro-posts were structured on the wafers through a standard photolithography and etching process, as illustrated in Fig. 1(a). After the processing steps, surfaces with a post height of 15 ± 1 μ m and pitch of 16 ± 0.5 μ m were obtained. Two post diameters were considered, 12 ± 0.5 μ m and 7 ± 0.5 μ m, yielding cavity fractions (f_c) of 0.56 and 0.85, respectively. To provide a baseline, a smooth silicon wafer without posts was used (f_c = 0). A chromium layer with a nominal thickness 100 nm was deposited on each silicon substrate to promote adhesion of a thin layer of Teflon,

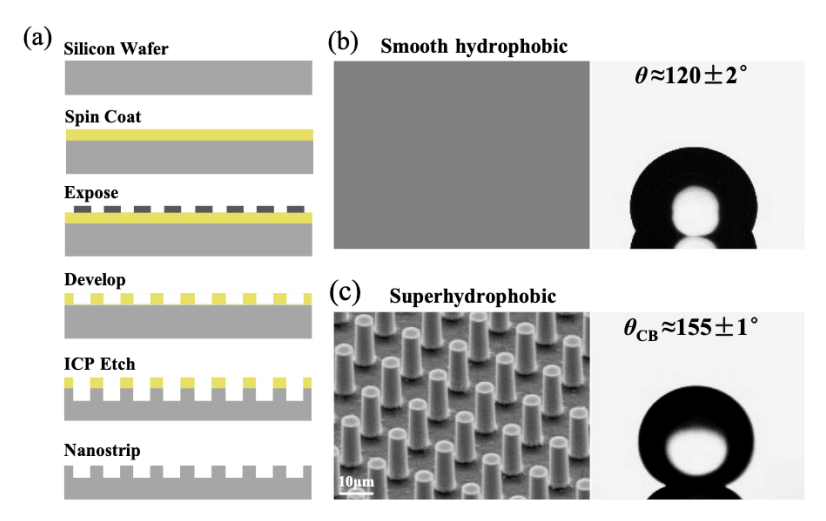


Fig. 1. (a) Illustration of the standard fabrication process steps to yield micro-posts on silicon wafers. (b) SEM image of smooth hydrophobic surface (left) and image of a water droplet on the smooth hydrophobic surface (right). (c) SEM image of a micro-post structured surface (left) and image of a water droplet on the SH surface P16D07 (right).

which was subsequently applied through a spin coating process. The Teflon solution was made by dissolving Teflon (4, 5-difluoro-2,2-bis(trifluoromethyl)-1,3-dioxole) in FC-40. After spin coating, the thickness of the Teflon layer was nominally 200 nm. The wafers were then heated to 90 °C for 5 min, 165 °C for 5 min and 330 °C for 20 min to provide robust adhesion. The combination of microscale posts and a Teflon coating renders the surfaces superhydrophobic, which is often characterized by the static contact angle. Using image processing techniques, the static contact angles of $\sim 5~\mu L$ water droplets on the fabricated surfaces were measured to be $120 \pm 2^{\circ}$ on the smooth hydrophobic surface, $140 \pm 1^{\circ}$ on the surface with posts of 12 μm diameter (P16D12), and 155 \pm 1° on the surface with posts of 7 µm diameter (P16D07). Representative scanning electron microscope (SEM) images of the surfaces and water droplets indicating static contact angles are shown in Fig. 1(b) and (c).

2.2. Experimental procedure

Droplet impact experiments were conducted using the setup illustrated in Fig. 2. Silicon wafers were attached to an aluminum block, using thermal paste to minimize contact resistance, with two 500 W cartridge heaters embedded. A thermocouple was placed immediately below the silicon wafers, also embedded in

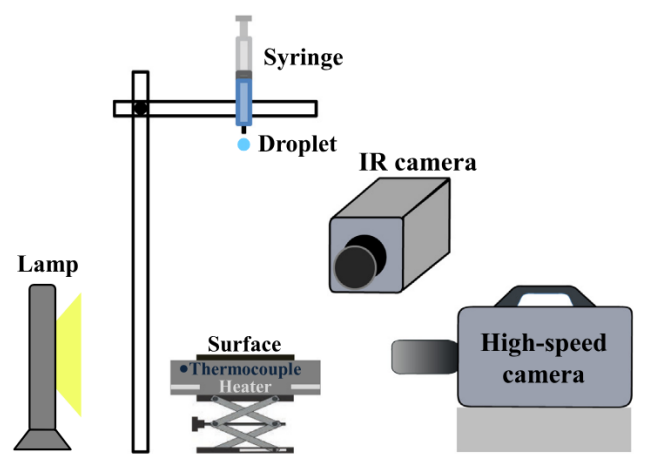


Fig. 2. Schematic of the setup for droplet impingement experiments.

the aluminum block. A high speed video camera (Photron SA4), operating at 5,000 fps and a high speed infrared camera (FLIR SC6100), operating at 800 fps were used to record the dynamic process and corresponding temperature distribution through time. The domain that was imaged using the high-speed video and IR cameras corresponded to pixel arrays of 512 × 1024 pixels and 160 × 128 pixels, respectively. This yields spatial resolutions of 8.5×10^{-3} mm/pix (horizontal) and 4.3×10^{-3} mm/pix (vertical) for the video camera and 2.7×10^{-2} mm/pix (horizontal) and 3.4×10^{-2} mm/pix (vertical) for the IR camera. The IR camera was calibrated as follows. Water was heated in a well-stirred pool. A K-type thermocouple was positioned 1 mm below the surface of the pool and the top surface of the pool was imaged with the IR camera. An emissivity value of $\epsilon = 0.95$ was input to the IR camera to identically match the thermocouple and IR camera measurements at a pool temperature of nominally 50 °C. Subsequently, the pool temperature was gradually decreased and the IR camera and thermocouple temperature measurements were recorded over the entire cooling process. Over the entire temperature range from 20 to 50 °C, the difference between the thermocouple and IR camera measurement was than ±0.3 °C. A flat black surface of emissivitv 0.94–0.98 was maintained at $50\pm1\,^{\circ}\text{C}$ and used as a background for the IR imaging. The temperature of the block was carefully controlled using a Matlab program.

Deionized water droplets at room temperature were released from a fine gauge needle. The initial height of droplets from the wafers was adjusted to change the droplet impact velocity, v_0 . The dimensionless Weber number is defined as $We = \rho v_0^2 D_0/\gamma$, where $\rho = 998 \text{ kg/m}^3$ and $\gamma = 0.072 \text{ N/m}$ are the density and surface tension of water, respectively. In the experiments, the temperature change of the impacting droplet was less than 10 °C. This gives rise to a negligibly small change in water surface tension. Experiments were conducted at three Weber numbers (We = 20, 30 and 40), three droplet diameters ($D_0 = 2.0$, 2.3, 2.9 mm) and on the three surfaces described above. At least six trials were realized and analyzed for each scenario to reduce the random error.

2.3. Droplet temperature measurement

Instantaneous temperature data from the IR camera was processed in Matlab. Due to the surface curvature of droplets, the apparent measured droplet temperature from the IR images

exhibits artificially high (and consistent) temperatures near the edges of the droplet. The emissivity of water droplets is essentially constant from the normal direction to a Brewster angle of about 50°. Therefore, the central part of the droplet surface can be approximated as Lambertian and the temperature values in the center region accurately represent the temperature of the impacting droplet [37]. A threshold range of nominally 23-45 °C was set in the camera software to remove the hot background (50 $^{\circ}$ C) and the underlying hot substrate (60 $^{\circ}\text{C})$ from the IR images. This was done to obtain better imaging of the droplet center. To reduce random error, an average temperature was computed by averaging over many pixels surrounding the center of the droplet. In all cases the averaging was contained to a region that represented nominally the inner 20% of the imaged droplet. For the droplets of diameter $D_0 = 2.3$ mm this area corresponds to about 100 pixels and the measured bulk droplet temperature was insensitive to the number of pixels in the averaging domain provided the number was larger than about 10-20 and smaller than about 200. When the averaging domain was too large, curvature effects of the outer region of the droplet introduce an artificial enhancement to the measurement. This occurred when the size of the averaging area was above nominally 50% of the imaged droplet.

A representative temperature variation of a droplet impacting the surfaces is shown in Fig. 3. Before impact, the measured droplet temperature remains constant and is defined as the initial droplet temperature T_{d0} . During contact the temperature initially rises as the droplet spreads then falls as it retracts and detaches. After detaching from the surface, there is a spike in temperature which is an artifact of droplet distortion. The measured average temperature continues to vary slightly with time as the drop moves vertically and then falls back toward the surface. This variation is caused by: (1) internal mixing in the droplet; and (2) distortion of the droplet shape as it deforms. In all cases considered here, as the droplet falls back to the surface the variation in temperature is minimized as it has a very nearly spherical shape and the mixing process is so rapid as to cause essentially uniform droplet temperature. Thus, the final droplet temperature, $T_{\rm df}$, is evaluated as the average value of the droplet temperature just prior to the second impingement event.

Due to the impact, deformation spreading, and retraction, convection dominates the internal heat transfer. The time scale associated with convection scales as the droplet diameter normalized by

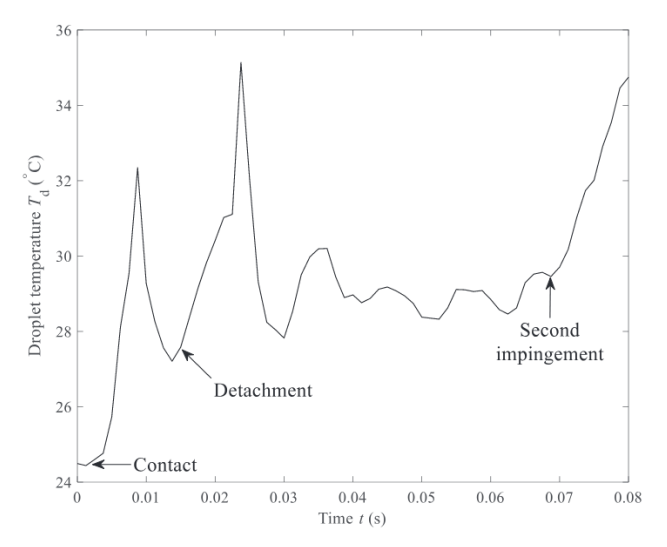


Fig. 3. Temperature variation of an impinging droplet (D_0 = 2.3 mm) on the smooth hydrophobic surface. The initial temperature of the surface is 80 °C and Weber number is 20.

the impact speed, and for the We = 20 cases this yields a convective time scale of approximately 2.3 ms. Note that this value is much lower than the time delay between initial and final images from which the overall temperature difference of the droplet is determined (approximately 50-60 ms).

At higher Weber numbers several small satellite drops are present after the main droplet detaches. When this occurs the weighted average of the fragment droplet temperatures and corresponding mass ratios is calculated as the effective $T_{\rm df}$. The overall cooling effectiveness is defined as the ratio of the actual heat transfer to the droplet to the maximum heat that could be transferred [10]. Accordingly, the experimental cooling effectiveness in this study is calculated as $\varepsilon = (T_{\rm df} - T_{\rm d0})/(T_{\rm w0} - T_{\rm d0})$.

2.4. Uncertainty analysis

The experimental uncertainties in this research primarily involve measurement of the impact Weber number and the overall cooling effectiveness. The initial diameter of the droplets is measured using a Matlab image analysis program. The accuracy of the initial drop diameter is ± 0.2 mm. The impact velocity was changed by adjusting the droplet release height, H. Measurement of H has an error of ± 0.5 mm. The experimental Weber number is calculated as $We = 2gHD_0\rho/\gamma$, where g is the acceleration of gravity. Therefore the uncertainty of Weber number is estimated as [38]

$$\left|\frac{U_{We}}{We}\right| = \sqrt{\left(\frac{U_H}{H}\right)^2 + \left(\frac{U_{D_0}}{D_0}\right)^2},\tag{1}$$

which ranges from $\sim 1.9\%$ to $\sim 3.2\%$ in this study.

The droplet temperature was measured as explained above and calculated by processing the thermal images. Due to the uncertainty of the emissivity and the accuracy of processing method, the measured temperature of the droplets before and after impingement has an error of ± 0.5 °C for each trial. The wall temperature was measured by a thermocouple with a measurement error of ± 0.2 °C. The uncertainty of the experimental cooling effectiveness for a single trial can be evaluated as

$$\left| \frac{U_{\varepsilon}}{\varepsilon} \right| = \sqrt{\left(\frac{U_{T_{df}}}{T_{df} - T_{d0}} \right)^2 + \left(\frac{U_{T_{w0}}}{T_{w0} - T_{d0}} \right)^2 + \left(\frac{U_{T_{d0}}}{T_{df} - T_{d0}} - \frac{U_{T_{d0}}}{T_{w0} - T_{d0}} \right)^2}.$$
(2)

For each scenario, six trials are performed to reduce the uncertainty and an average cooling effectiveness is computed. The uncertainty is smallest for the scenario where the initial temperature difference between the droplet and surface is greatest and the measured temperature change of the droplet is greatest, according to Eq. (2). For an impacting droplet, the measured temperature change is clearer for smaller droplet diameter, higher substrate temperature, and higher Weber number. For $We = 20, D_0 = 2.9$ mm and $T_s = 50$ °C, the uncertainty value is highest at 26.5%. For $We = 40, D_0 = 2.0$ mm and $T_s = 90$ °C, the uncertainty value is lowest at 3.4%. Thus, $|U_{\epsilon}/\epsilon|$ has a range of $\sim 3.4\%$ to $\sim 26.5\%$, depending on the specific experimental parameters.

3. Theoretical analysis

3.1. Contact area approximation

To calculate the liquid contact area with the underlying surface, the temporal spreading diameter of the droplet D(t) is needed. The spreading ratio $\beta(t) = D(t)/D_0$ is usually used to express the spreading and retraction of the droplet. Considering the free-slip scenario on SH surfaces, it is reported that the initial surface energy

and about half of the initial kinetic energy are transformed into the final surface energy [39]. The initial surface energy of the droplet before impact is $E_{\rm s,0}=\pi D_0^2\gamma$, and the initial kinetic energy is $E_{\rm k}=\frac{1}{12}\pi\rho D_0^3 v_0^2$. The interfacial energy of the droplet at maximum spreading is $E_{\rm s,max}=\frac{1}{4}\pi D_{\rm max}^2(1-\cos\theta_{\rm CB})\gamma$. Solving the energy equation $E_{\rm s,0}+\frac{1}{2}E_{\rm k}=E_{\rm s,max}$, the maximum spreading ratio is expressed as

$$\beta_{\text{max}} = \sqrt{\frac{4}{1 - \cos \theta_{\text{CB}}} \left(\frac{1}{24} We + 1\right)}.$$
 (3)

The Cassie-Baxter contact angle of droplets on the SH surfaces can be predicted as $\cos\theta_{\rm CB}=(1-f_c)\cos\theta_0+f_c\cos180^\circ=(1-f_c)\cos\theta_0-1$, where θ_0 is the contact angle on a smooth hydrophobic surface [40]. Previous research indicates that the contact time between the droplet and a SH surface scales as $\sqrt{\rho r_0^3/\gamma}$, which is independent of Weber number [23]. For the Leidenfrost droplets where the contact angle is assumed as $\theta_{\rm CB}=180^\circ$, the contact time is about $t_{\rm osc}=\pi\sqrt{\rho r_0^3/2\gamma}$, which is the lowest-order oscillation period [4]. To express the effect of the contact angle, the contact time of bouncing droplets on SH surfaces is approximated as [41]

$$t_{\text{contact}} = \frac{\pi}{2\sqrt{2(1-\cos\theta_{\text{CB}})}} \sqrt{\frac{\rho D_0^3}{\gamma}}.$$
 (4)

The time of maximum spread, $t_{\rm max}$, of Leidenfrost droplets is reported to behave approximately as $t_{\rm osc}/3$ with little difference between the liquids [42,43]. Therefore, in this paper the spreading ratio is approximated as

$$\beta(t) = \frac{27}{4} \beta_{\text{max}} \frac{t}{t_{\text{contact}}} \left(1 - \frac{t}{t_{\text{contact}}}\right)^{2}. \tag{5}$$

Then the contact area between the bouncing droplet and the underlying surface is $A(t) = \frac{1}{4}\pi D_0^2 \beta(t)^2$.

3.2. Heat flux solution

For single phase impact of droplets on solid surfaces, the axisymmetric flow field inside the impacting droplet can be approximately defined as an inviscid flow, which is defined as [14,12,44]

$$u_{\rm r} = \frac{\rm r}{t}, \quad u_{\rm z} = \frac{-2z}{t}. \tag{6}$$

A thermal energy balance in the droplet yields

$$\frac{\partial T_{\rm f}}{\partial t} + \boldsymbol{u} \nabla T_{\rm f} - \alpha_{\rm f} \nabla^2 T_{\rm f} = 0. \tag{7}$$

Using the velocity profile (6), the energy equation in (7) can be simplified as

$$\frac{\partial T_f}{\partial t} - \frac{2z}{t} \frac{\partial T_f}{\partial z} - \alpha_f \frac{\partial^2 T_f}{\partial z^2} = 0. \tag{8} \label{eq:8}$$

Introducing the similarity variable $\eta = \frac{z}{2\sqrt{\alpha_t t'}}$ an ordinary differential equation for the temperature field $T_{\rm f} = T_{\rm f}(\eta)$ is derived as

$$T_{\rm f}'' + 5\eta T_{\rm f}' = 0. {9}$$

Initial and boundary conditions are

$$T_{\rm f} = T_{\rm interface}$$
 at $\eta = 0$; $T_{\rm f} = T_{\rm d0}$ at $\eta \to \infty$. (10)

The similarity solution of the above equations is

$$T_{\rm f}(z,t) = T_{\rm interface} + (T_{\rm d0} - T_{\rm interface}) \operatorname{erf}(\frac{\sqrt{5}z}{2\sqrt{\alpha_{\rm f}t}}). \tag{11}$$

Using Fourier's law, the heat flux at the liquid/solid interface is calculated as

$$q_{\rm f}''(t) = k_{\rm f} \frac{\partial T_{\rm f}}{\partial z}\Big|_{z=0} = \frac{\sqrt{5}e_{\rm f}(T_{\rm interface} - T_{\rm d0})}{\sqrt{\pi t}},$$
 (12)

where $e_f = \sqrt{k_f \rho_f c_{p,f}}$ is the thermal effusivity of the water droplets. The transient heat conduction in the semi-infinite solid wall during droplet impact is expressed as

$$\frac{\partial T_{\rm w}}{\partial t} - \alpha_{\rm w} \frac{\partial^2 T_{\rm w}}{\partial z^2} = 0, \tag{13}$$

with initial and boundary conditions

$$T_{\rm w} = T_{\rm interface}$$
 at $z = 0$; $T_{\rm w} = T_{\rm w0}$ at $z \to -\infty$. (14)

Solving (12) subject to (13), the heat flux at the solid/liquid interface is

$$q_{\rm w}^{"}(t) = k_{\rm w} \frac{\partial T_{\rm w}}{\partial z}\Big|_{z=0} = \frac{e_{\rm w}(T_{\rm w0} - T_{\rm interface})}{\sqrt{\pi t}},$$
 (15)

where $e_{\rm w}$ is the thermal effusivity of the wall. Using the relationship between the heat fluxes at the interface $q_{\rm f}^{''}(t)=q_{\rm w}^{''}(t)$, the interface temperature is derived as

$$T_{\text{interface}} = \frac{\sqrt{5}e_{\text{f}}T_{\text{d0}} + e_{\text{w}}T_{\text{w0}}}{\sqrt{5}e_{\text{f}} + e_{\text{w}}}.$$
 (16)

Then the heat flux to the droplet at the interface is expressed as

$$q_{\rm f}''(t) = \frac{\sqrt{5}e_{\rm f}e_{\rm w}(T_{\rm w0} - T_{\rm d0})}{(\sqrt{5}e_{\rm f} + e_{\rm w})\sqrt{\pi t}}.$$
 (17)

For droplet impact on SH surfaces, the solid surface is treated as a composite wall with silicon posts and air, of which the effective thermal effusivity is $e_{\rm w}=\sqrt{k_{\rm w}\rho_{\rm w}c_{\rm p,w}}$. Using the thermal resistance approach, the thermal conductivity of the composite wall is calculated as $k_{\rm w}=k_{\rm sil}(1-f_c)+k_{\rm air}f_c$. Additionally, the volumetric specific heat capacity of the wall can be approximated as $\rho_{\rm w}c_{\rm p,w}=\rho_{\rm sil}c_{\rm p,sil}(1-f_c)+\rho_{\rm air}c_{\rm p,air}f_c$ [45,46]. Table 1 summarizes the thermophysical properties of materials used in this study.

We note here the contact time is the most important time scale in calculating the total heat exchange between the impinging drop and the substrate. As has been show previously, heat transfer mainly occurs during the droplet spreading stage, while it decreases with time [10,13]. While the droplet is spreading the transport is dominated by unsteady stagnation conditions (i.e. decreasing impact velocity with time). Here the wall transfers heat to the droplet following classical stagnation point flow behavior. Once the drop has spread to its maximum radius, the rim of the drop starts to recede. However, the core of the drop is continuing its outward motion and the rim moves inward as a free-surface wave. During the retraction phase the amount of heat transfer is greatly reduced due to 1) the drop is now moving back inward over already cooled solid surface; 2) the bottom portion of the drop (thermal penetration distance) has already been heated during the spreading phase. In this study we have simplified the analysis

Table 1Thermophysical properties of materials.

Properties	Water (f)	Silicon (sil)	Air (air)
$\rho (kg/m^3)$	998	2329	1.29
$c_{\rm p} ({\rm J/kg} \ {\rm K})$	4200	700	1006
k(W/m K)	0.6	120	0.026

to make it tractable by assuming in the thermal transport model that stagnation point flow dynamics prevail within the droplet over the entire contact time.

3.3. Cooling effectiveness calculation

To express the heat transfer capacity to an impinging droplet, the dimensionless cooling effectiveness $\varepsilon=Q/mc_{\rm p,f}(T_{\rm w0}-T_{\rm d0})$ is calculated theoretically [10]. For droplet impingement, the time is usually normalized as $\hat{t}=t\,\nu_0/D_0$, and thus the normalized contact time is

$$\hat{t}_{contact} = \frac{t_{contact}}{D_0/v_0} = \frac{\pi\sqrt{We}}{2\sqrt{2(1-\cos\theta)}}.$$
 (18)

The total heat transfer to the bouncing droplet during the contact period can be calculated as

$$Q = \int_{0}^{t_{\text{contact}}} q_{\text{f}} \prime \prime (t) A(t) dt = \int_{0}^{\hat{t}_{\text{contact}}} q_{\text{f}} \prime \prime (\hat{t}) A(\hat{t}) D_0 / \nu_0 d\hat{t}$$
 (19)

Finally, the defined cooling effectiveness of a bouncing droplet is expressed as

$$\epsilon\!=\!\frac{3}{2D_{0}\rho_{\mathrm{f}}c_{\mathrm{p,f}}}\int_{0}^{\hat{t}_{\mathrm{contact}}}\frac{\sqrt{5}e_{\mathrm{f}}e_{\mathrm{w}}}{\left(\sqrt{5}e_{\mathrm{f}}+e_{\mathrm{w}}\right)\sqrt{\pi\hat{t}}}\!\left(\!\frac{27}{4}\beta_{\mathrm{m}}\frac{\hat{t}}{\hat{t}_{\mathrm{contact}}}\!\left(1-\frac{\hat{t}}{\hat{t}_{\mathrm{contact}}}\!\right)^{2}\right)^{2}\sqrt{\frac{D_{0}}{\nu_{0}}}d\hat{t}$$

4. Results and discussion

4.1. Visualization of impinging droplets

Image sequences of impinging droplets, with initial diameter $D_0 = 2.3$ mm, on a smooth hydrophobic and each SH surface, P16D12 and P16D07, recorded by the high-speed video and IR camera are shown in Fig. 4(a), (b), and (c), respectively. Images are shown at seven times during the impingement process, starting at impact and moving through to droplet detachment. The surface temperature is 60 °C and the Weber number is 20. Note that the

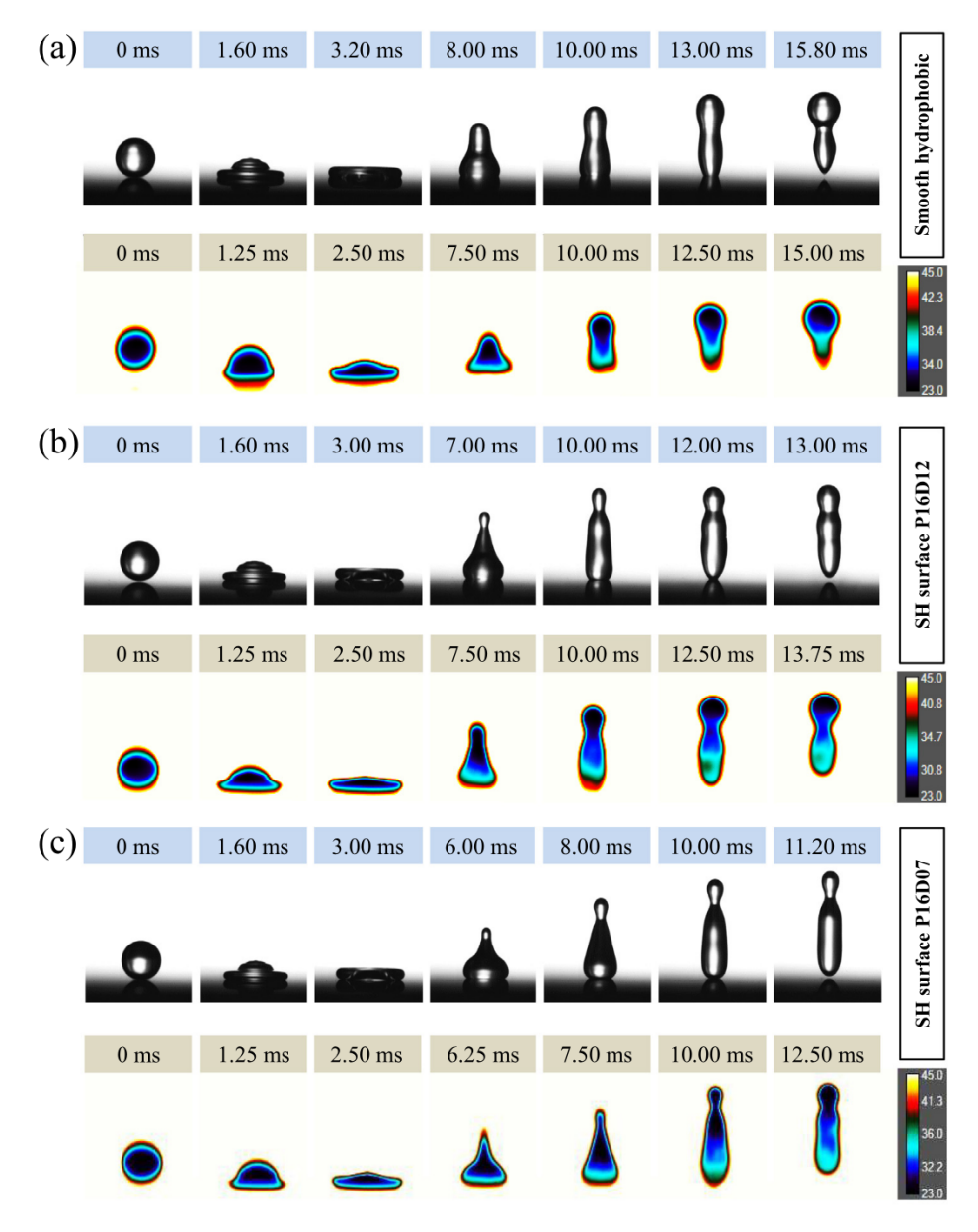


Fig. 4. Image sequence of bouncing droplets of D_0 = 2.3 mm on (a) the smooth hydrophobic surface, (b) the SH surfaces P16D12, and (c) the SH surfaces P16D07. The initial temperature of the surfaces is 60° and the Weber number is 20.

0.012

0.014

0.012

0.012

0.01

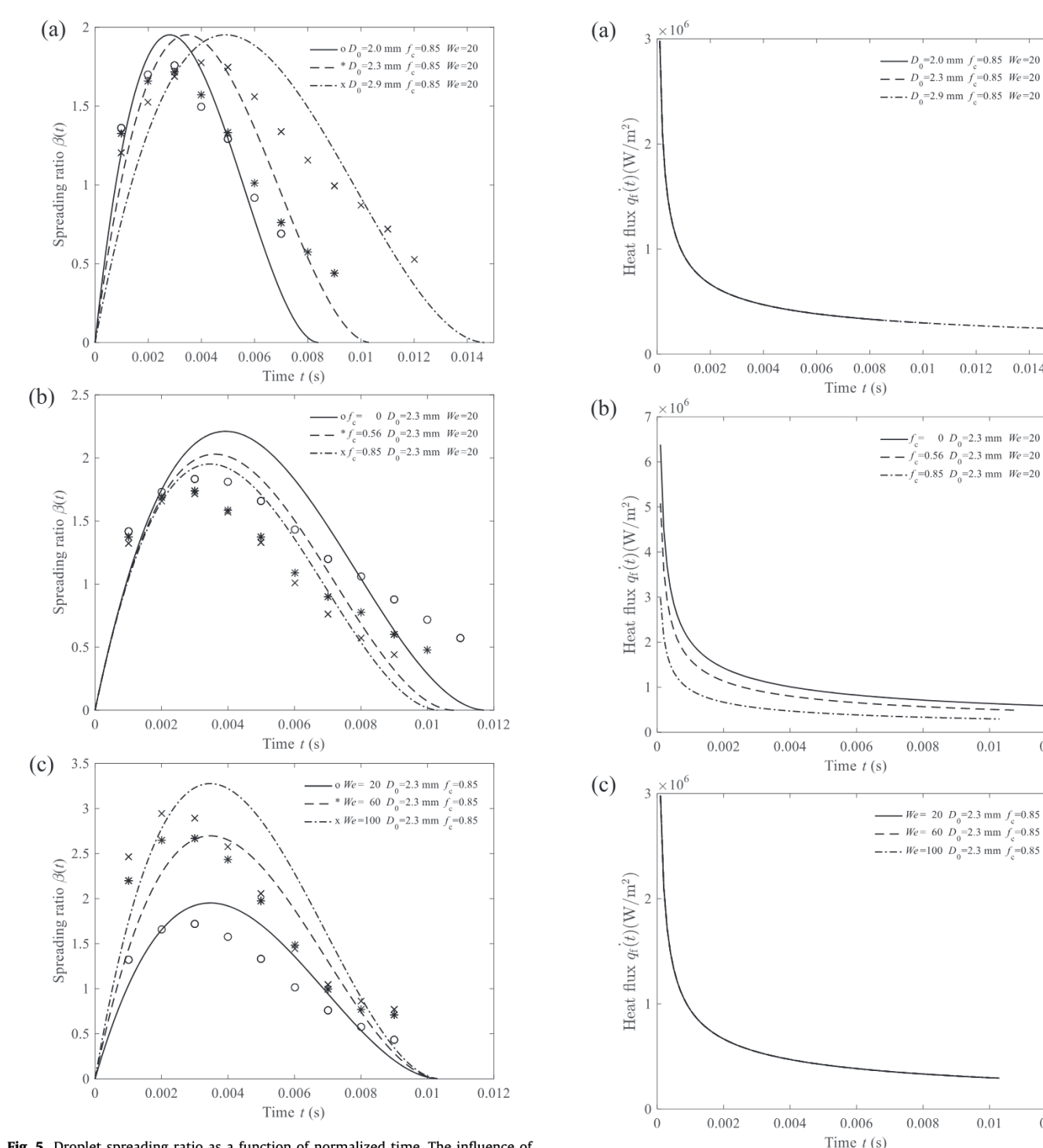


Fig. 5. Droplet spreading ratio as a function of normalized time. The influence of droplet diameter D_0 , cavity fraction f_c , and Weber number We is shown in panel a, b, and c, respectively.

time stamps for the IR and visible images do not exactly correspond due to the differing frame rates of the instruments. It is observed that the droplets bounce off all three surfaces after the spreading and retraction stages. The total contact time of the impacting drops is shorter on the surface with a higher cavity fraction. On these surfaces the droplet retracts more quickly because the friction resistance between the droplet and the underlying substrate is less and the contact angle is higher. Corresponding

Fig. 6. Heat flux to an impinging droplet as a function of time. The influence of droplet diameter D_0 , cavity fraction f_c , and Weber number We is shown in panel a, b, and c, respectively.

thermal images provide temporally and spatially resolved temperature information for the exterior surface of the droplet. It can be qualitatively judged that the droplet is heated by the underlying surface and the heat is accumulated in the droplet during the contact period, as the droplet is filled with brighter colors. To quantify the heat transfer to droplets and the effect of parameters, theoretical predictions are presented and further compared with experimental results.

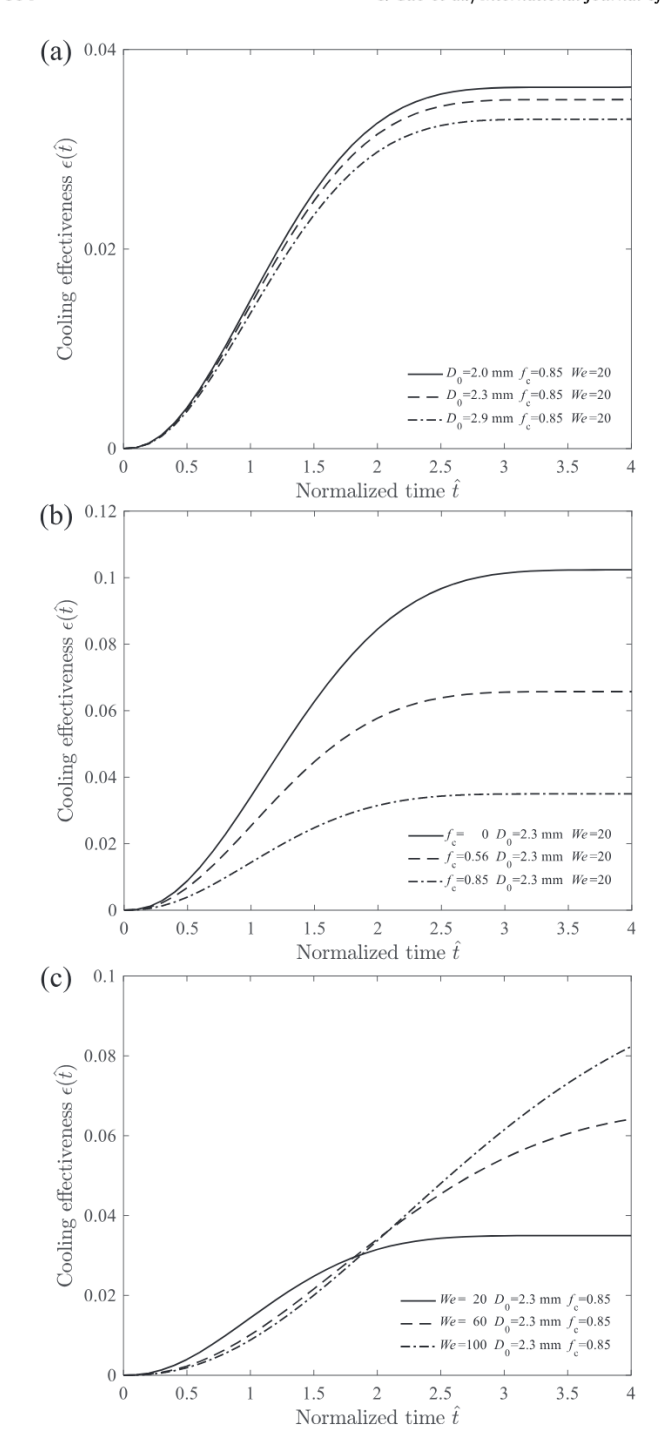


Fig. 7. Cooling effectiveness as a function of normalized time. The influence of droplet diameter D_0 , cavity fraction f_c , and Weber number We is shown in panel a, b, and c, respectively.

4.2. Theoretical predictions

The effect of initial droplet diameter D_0 , cavity fraction f_c , and Weber number We on the variation of the droplet spreading ratio with time is shown in Fig. 5. In Fig. 5a the cavity fraction is held constant at f_c = 0.85 and the Weber number is held at 20 while the droplet diameter is varied from 2.0 mm to 2.9 mm. Similarly, in Fig. 5b the droplet diameter and Weber number are held constant while f_c varies and in Fig. 5c We is varied while the other two parameters remain constant. Note the maximum value of

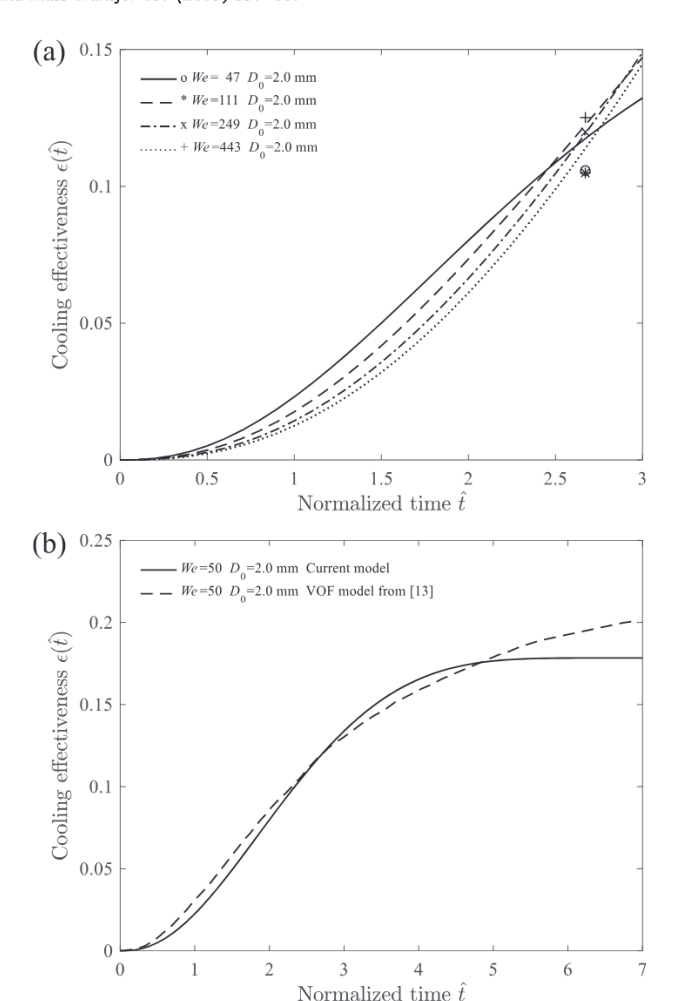


Fig. 8. Comparison of current model with previous simulations. In (a), the present predictions are shown by lines and the results of Pasandideh-Fard et al. [10] are shown by markers. In (b), the present predictions are shown by a solid line and the prior VOF results of Strotos et al. [13] are shown with the dashed line.

the spreading ratio does not change with D_0 due to the normalization. The theoretical maximum spread diameter does, however, decrease with increasing f_c . This is due to the increasing Cassie-Baxter contact angle that appears in Eq. (3), which is manifest as an increasing interfacial surface tension energy. Conversely, $\beta_{\rm max}$ increases with increasing We, due to the increasing initial kinetic energy. In addition to the spreading ratio, the variation in total contact time is also reflected in the panels of Fig. 5. The model predictions show a contact time that is independent of We, but increases with increasing D_0 and decreases with increasing f_c .

Also shown in the panels of Fig. 5 are results derived from the high speed video imaging. Here the experimental spreading ratios are shown with symbols and data were acquired at the same parameter values as the model predictions. In general, the experimental data show similar β vs. time trends. However, for all cases the maximum value of β is smaller for the experiments and the spreading and retraction times are longer. This occurs because the model neglects viscous losses. Thus, the actual distance the droplet spreads and the rate of spreading/retraction are lower for the experimental data.

The effect of D_0 , f_c , and We on the variation of heat flux with time from the model is illustrated in Fig. 6, where predictions are shown for the same scenarios as shown in Fig. 5. For all scenarios, the initial temperature difference between the droplet and the wall is 40 °C. The heat flux decreases with time due to the increasing

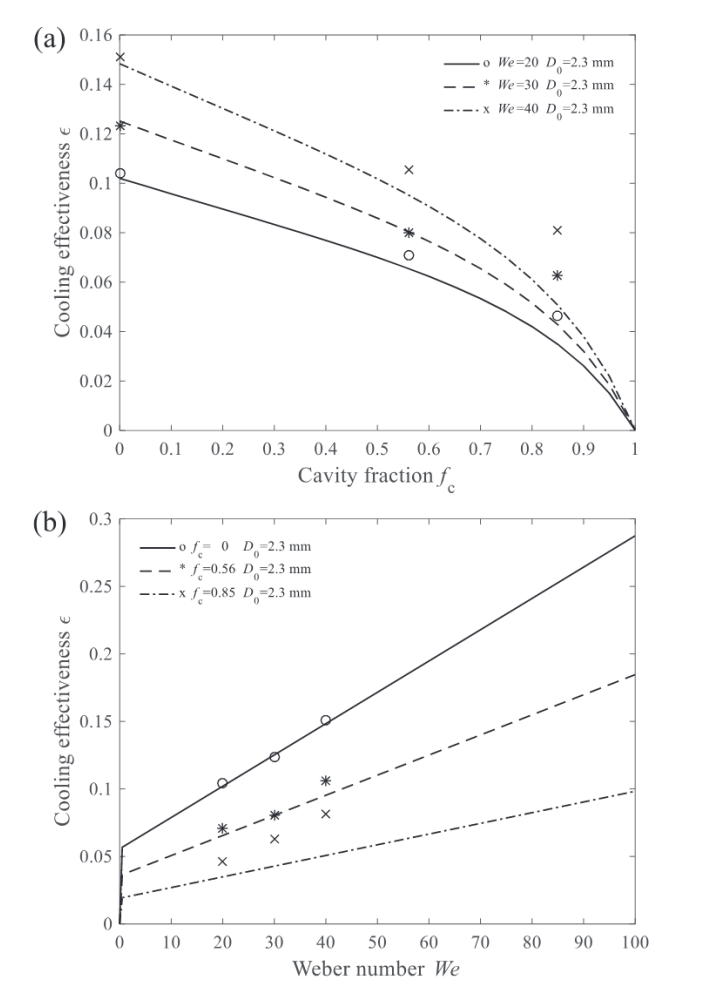


Fig. 9. Comparison of theoretical (lines) and experimental (markers) values of the total cooling effectiveness ϵ as a function of f_c in (a), and as a function of We in (b).

thermal diffusion length inside both the droplet and the wall. Because the velocity profile assumed is independent of droplet size and impact velocity, the predicted heat flux does not change with variations in either D_0 and We. In previous numerical simulations, the impact velocity was shown to only weakly affect the heat flux [10,19]. The heat flux decreases with surface cavity fraction, because the increasing fraction of the surface that is covered by air-filled cavities leads to a reduced thermal diffusivity at the composite wall.

Predictions of the overall cooling effectiveness, ϵ , and its dependence on D_0, f_c , and We is now considered. ϵ is shown in Fig. 7 as a function of the normalized time in three panels, with f_c , We, and D_0 values varied in the same manner as Fig. 5. Also shown in the panels are the normalized times when the droplet has reached maximum expansion. For all cases the cooling effectiveness increases with time as thermal energy is transferred to the droplet during the spreading/retraction process. Note that greater than 90% of the thermal transport to the droplet occurs during the expansion process. ϵ increases with increasing We due to both increasing fluid speed and increased total contact area. However, the predictions shown in panel b reveal a marked decrease in ϵ with increasing f_c . This is caused by a reduction in the heat flux due to: 1) smaller total droplet contact time with the surface (i.e. panel b of Fig. 5); and 2) the increased thermal resistance caused by air-filled cavities on the surface. For a droplet with a larger diameter, the droplet mass increase is more significant, resulting in lower cooling effectiveness.

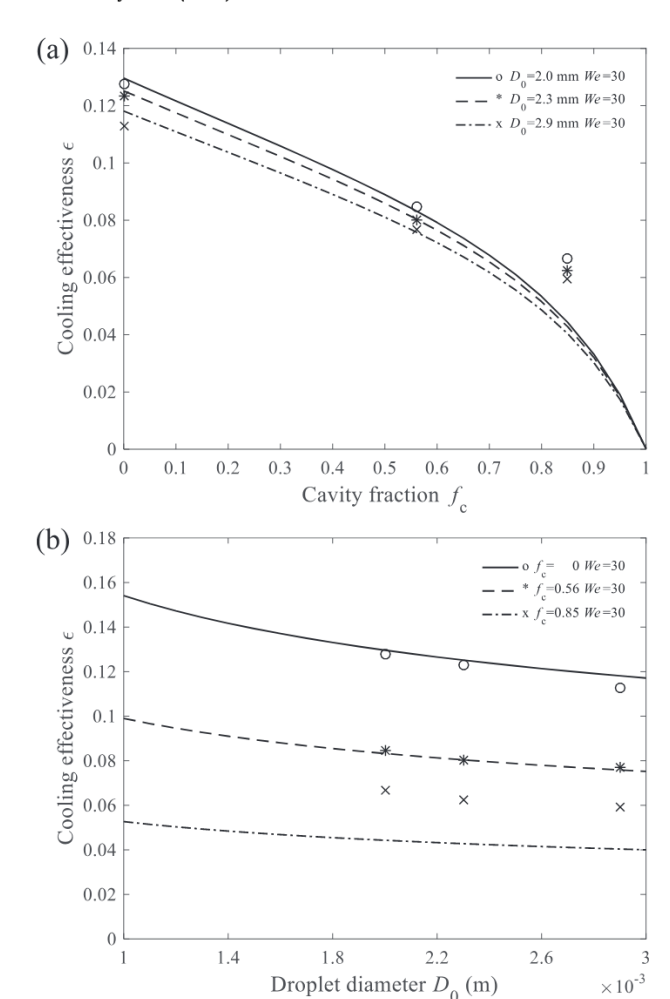


Fig. 10. Comparison of theoretical (lines) and experimental (markers) values of the total cooling effectiveness ϵ as a function of f_c in (a), and as a function of D_0 in (b).

The current cooling effectiveness model predictions are compared to prior VOF model results from Pasandideh-Fard et al. [10] for a surface that was not superhydrophobic in Fig. 8(a). The prior VOF results are shown as symbols at four conditions as shown in the figure legend. These results are only available at the condition of maximum spreading, determined to be $\hat{t}=8/3$ in [10]. At this time, the calculated cooling effectiveness from the current model shows good agreement with the VOF simulations. An overestimate of the maximum spreading time can be seen in the model in Fig. 5. This corresponds to each of the points in the VOF model being shifted to the right in Fig. 8(a), resulting in all cooling effectiveness estimates being overestimates, due to the enhanced spreading from the inviscid assumption.

Results from the current model are also compared to the variation in cooling effectiveness with time as predicted by Strotos et al. [13], who also employed the VOF method. This comparison is shown in Fig. 8(b). Note that in both prior VOF models considered, the droplets do not rebound from the stainless steel substrates since the surface is hydrophilic, although a slight retraction does occur. The comparison of the present analytical model results with the two prior VOF models reveal similar results when determining the overall cooling effectiveness. Seen from Fig. 8(b), the current model has similar predictions but the values are lower at the spread stage, concomitant with the slower initial spreading seen in Fig. 5, then greater where spreading is overestimated. Then the cooling effectiveness tends to be constant with the further increase of time. This is caused by the reduced contact area

between the smooth hydrophobic surface and bouncing droplets at the retraction stage, which is quite different from that on a hydrophilic substrate as presented in [13].

4.3. Theoretical and experimental heat transfer

Values of the total cooling effectiveness derived from the theoretical model and the experimental measurements are compared in Figs. 9 and 10. Here ϵ is determined after the droplet has rebounded from the surface for the experiments and after the retraction process for the theoretical model. Solid lines represent the theoretical predictions and experimental results are represented with symbols. The data of Fig. 9 correspond to conditions with a fixed droplet size of $D_0 = 2.3$ mm. Fig. 9(a) provides ϵ as a function of cavity fraction at three impingement Weber numbers and Fig. 9(b) shows ϵ as a function of Weber number for three cavity fractions.

As expected, the data reveal that the cooling effectiveness decreases with cavity fraction, due to the existence of the insulating trapped air in the cavity regions. At cavity fractions less than 0.8, ϵ decreases approximately linearly with increasing f_c , where at high cavity fractions the decrease in ϵ is much more dramatic. Increasing We also yields an increase in ϵ due to increased droplet spreading and fluid speed. The increased spreading diameter increases the interfacial contact between the liquid and the solid surface and the increased speed increases the convection, especially important near the stagnation zone.

At lower cavity fraction, $f_c=0$ and 0.56, the experiments and theoretical model results show very good agreement. However, at $f_c=0.85$, the model under predicts the cooling effectiveness of the experiments, although the general trends remain similar. High speed imaging of the droplet viewed from above reveals that localized wetting (penetration into the cavities) occurs near the stagnation point on the higher cavity fraction surface and this region increases with increasing Weber number. In the wetting region the surface contact area increases and this is likely the cause for the increase in ϵ in the experiments.

For completeness, the influence of droplet diameter is shown in Fig. 10, where model and experimental results are shown in Fig. 10 (a) (ϵ vs. f_c) and Fig. 10(b) (ϵ vs. D_0). Again, the model and experimental results have similar trends and for f_c = 0 and 0.56 the agreement is very good. The increase in cooling effectiveness at f_c = 0.85 likely occurs because of the wetting phenomenon proposed above. When smaller droplets impact the surface, the cooling effectiveness is larger due to the decreased thermal capacitance of small droplets.

5. Conclusions

Heat transfer to bouncing liquid droplets on superhydrophobic surfaces was studied in this paper. Experiments were performed using a combination of high speed and IR imaging to capture the droplet impact dynamics and corresponding heat transfer process. Further, a similarity solution model was employed to predict the instantaneous heat flux at the interface (and total heat transfer to the droplet) based on an assumed inviscid flow inside the droplet. Fluid convection has been taken into account in the model, which enhances the heat flux compared with a simplified model of transient heat conduction between two semi-infinite bodies. In the model, the superhydrophobic surface is treated as a composite wall of solid posts and air. Approximations of instantaneous droplet spreading diameter and total contact time are utilized in the model. The heat flux decreases with time and as the surface cavity fraction is increased, while the droplet diameter and impact velocity have smaller influence. The total heat transferred to a droplet

during the impact, spreading, and retraction events is calculated to yield an overall theoretical cooling effectiveness. Thermal imaging allows measurement of the bulk temperature change of impinging droplets and thus an experimental cooling effectiveness was also determined. The cooling effectiveness increases with increasing Weber number but decreases with increasing droplet diameter and surface cavity fraction. The decrease in heat transfer as a function of the surface cavity fraction is an entirely new result and the model and experimental results document the decrease for Weber numbers in the range 20–40 and droplets ranging in diameter from 2.0 mm to 2.9 mm. The model and experimental results show the same qualitative trends and generally good agreement in cooling effectiveness values.

Declarations of interest

None.

Acknowledgement

This research is supported by the U.S. National Science Foundation (NSF) (Grant No. CBET- 1707123) and the China Scholarship Council (CSC).

Appendix A. Supplementary material

Supplementary data associated with this article can be found, in the online version, at https://doi.org/10.1016/j.ijheatmasstransfer. 2019.03.103.

References

- [1] J. Kim, Spray cooling heat transfer: the state of the art, Int. J. Heat Fluid Flow 28 (4) (2007) 753–767.
- [2] A.L.N. Moreira, A.S. Moita, M.R. Panão, Advances and challenges in explaining fuel spray impingement: how much of single droplet impact research is useful?, Prog Energy Combust. Sci. 36 (5) (2010) 554–580.
- [3] G. Liang, I. Mudawar, Review of drop impact on heated walls, Int. J. Heat Mass Transf. 106 (2017) 103–126.
- [4] L.H.J. Wachters, N. Westerling, The heat transfer from a hot wall to impinging water drops in the spheroidal state, Chem. Eng. Sci. 21 (11) (1966) 1047–1056.
- [5] J.D. Bernardin, C.J. Stebbins, I. Mudawar, Mapping of impact and heat transfer regimes of water drops impinging on a polished surface, Int. J. Heat Mass Transf. 40 (2) (1997) 247–267.
- [6] J.H. Moon, M. Cho, S.H. Lee, Dynamic wetting and heat transfer characteristics of a liquid droplet impinging on heated textured surfaces, Int. J. Heat Mass Transf. 97 (2016) 308–317.
- [7] J. Breitenbach, I.V. Roisman, C. Tropea, Drop collision with a hot, dry solid substrate: heat transfer during nucleate boiling, Phys. Rev. Fluids 2 (7) (2017) 074301.
- [8] J.D. Bernardin, I. Mudawar, Transition boiling heat transfer of droplet streams and sprays, Int. J. Heat Mass Transf. 40 (11) (2007) 2579–2593.
- [9] M.A.J.V. Limbeek, M.H.K. Schaarsberg, B. Sobac, A. Rednikov, C. Sun, P. Colinet, D. Lohse, Leidenfrost drops cooling surfaces: theory and interferometric measurement, J. Fluid Mech. 827 (2017) 614–639.
- [10] M. Pasandideh-Fard, S.D. Aziz, S. Chandra, J. Mostaghimi, Cooling effectiveness of a water drop impinging on a hot surface, Int. J. Heat Fluid Flow 22 (2) (2001) 201–210
- [11] G. Strotos, G. Aleksis, M. Gavaises, K.S. Nikas, N. Nikolopoulos, A. Theodorakakos, Non-dimensionalisation parameters for predicting the cooling effectiveness of droplets impinging on moderate temperature solid surfaces, Int. J. Therm. Sci. 50 (5) (2011) 698-711.
- [12] I.V. Roisman, Fast forced liquid film spreading on a substrate: flow, heat transfer and phase transition, J. Fluid Mech. 656 (656) (2010) 189–204.
- [13] G. Strotos, N. Nikolopoulos, K.S. Nikas, K. Moustris, Cooling effectiveness of droplets at low weber numbers: effect of temperature, Int. J. Therm. Sci. 72 (10) (2013) 60–72.
- [14] J. Breitenbach, I.V. Roisman, C. Tropea, Heat transfer in the film boiling regime: single drop impact and spray cooling, Int. J. Heat Mass Transf. 110 (2017) 34– 42
- [15] S. Batzdorf, J. Breitenbach, C. Schlawitschek, I.V. Roisman, C. Tropea, P. Stephan, T. Gambaryan-Roisman, Heat transfer during simultaneous impact of two drops onto a hot solid substrate, Int. J. Heat Mass Transf. 113 (2017) 898–907.
- [16] L. Tarozzi, A. Muscio, P. Tartarini, Experimental tests of dropwise cooling on infrared-transparent media, Exp. Thermal Fluid Sci. 31 (8) (2007) 857–865.

- [17] J. Shen, C. Graber, J. Liburdy, D. Pence, V. Narayanan, Simultaneous droplet impingement dynamics and heat transfer on nano-structured surfaces, Exp. Thermal Fluid Sci. 34 (4) (2010) 496–503.
- [18] P. Dunand, G. Castanet, M. Gradeck, D. Maillet, F. Lemoine, Energy balance of droplets impinging onto a wall heated above the leidenfrost temperature, Int. J. Heat Fluid Flow 44 (4) (2013) 170–180.
- [19] M. Gradeck, N. Seiler, P. Ruyer, D. Maillet, Heat transfer for leidenfrost drops bouncing onto a hot surface, Exp. Thermal Fluid Sci. 47 (5) (2013) 14–25.
- [20] D. Chatzikyriakou, S.P. Walker, C.P. Hale, G.F. Hewitt, The measurement of heat transfer from hot surfaces to non-wetting droplets, Int. J. Heat Mass Transf. 54 (7) (2011) 1432–1440.
- [21] J. Jung, S. Jeong, H. Kim, Investigation of single-droplet/wall collision heat transfer characteristics using infrared thermometry, Int. J. Heat Mass Transf. 92 (2016) 774–783.
- [22] D. Richard, D. Quéré, Bouncing water drops, Epl 50 (6) (2000) 769.
- [23] D. Richard, C. Clanet, D. Quéré, Surface phenomena: contact time of a bouncing drop, Nature 417 (6891) (2002) 811.
- [24] D. Quéré, Wetting and roughness, Annu. Rev. Mater. Res. 38 (38) (2008) 71–99.
- [25] C.H. Chen, Q. Cai, C. Tsai, C.L. Chen, G. Xiong, Y. Yu, Z. Ren, Dropwise condensation on superhydrophobic surfaces with two-tier roughness, Appl. Phys. Lett. 90 (17) (2007) 53.
- [26] N. Miljkovic, R. Enright, E.N. Wang, Effect of droplet morphology on growth dynamics and heat transfer during condensation on superhydrophobic nanostructured surfaces, ACS Nano 6 (2) (2012) 1776–1785.
- [27] Z. Liu, Y. Gou, J. Wang, S. Cheng, Frost formation on a super-hydrophobic surface under natural convection conditions, Int. J. Heat Mass Transf. 51 (25) (2008) 5975–5982.
- [28] K.K. Varanasi, T. Deng, J.D. Smith, H. Ming, N. Bhate, Frost formation and ice adhesion on superhydrophobic surfaces, Appl. Phys. Lett. 97 (23) (2010), 234102–234102–3.
- [29] C.E. Clavijo, J. Crockett, D. Maynes, Hydrodynamics of droplet impingement on hot surfaces of varying wettability, Int. J. Heat Mass Transf. 108 (2017) 1714– 1726.
- [30] C.E. Clavijo, J. Crockett, D. Maynes, Thermally induced atomization during droplet impingement on superheated hydrophobic and superhydrophobic surfaces, Int. J. Heat Mass Transf. 126 (2018) 1357–1366.
- [31] R. Hays, D. Maynes, J. Crockett, Thermal transport to droplets on heated superhydrophobic substrates, Int. J. Heat Mass Transf. 98 (2016) 70–80.

- [32] A. Al-Sharafi, B.S. Yilbas, H. Ali, A. Al-Sharafi, B.S. Yilbas, H. Ali, A. Al-Sharafi, B. S. Yilbas, H. Ali, Droplet heat transfer on micro-post arrays: effect of droplet size on droplet thermal characteristics, Int. J. Heat Fluid Flow 68 (2017) 62–78.
- [33] A. Cowley, D. Maynes, J. Crockett, Effective temperature jump length and influence of axial conduction for thermal transport in superhydrophobic channels, Int. J. Heat Mass Transf. 79 (2014) 573–583.
- [34] M. Searle, D. Maynes, J. Crockett, Thermal transport due to liquid jet impingement on superhydrophobic surfaces with isotropic slip, Int. J. Heat Mass Transf. 110 (2017) 515–522.
- [35] G. Rosengarten, R. Tschaut, Effect of superhydrophobicity on impinging droplet heat transfer, in: International Heat Transfer Conference, 2010, pp. 741–746.
- [36] S. Shiri, J.C. Bird, Heat exchange between a bouncing drop and a superhydrophobic substrate, PNAS 114 (2017) 6930–6935.
- [37] H. Li, I.V. Roisman, C. Tropea, Influence of solidification on the impact of supercooled water drops onto cold surfaces, Exp. Fluids 56 (6) (2015) 133.
- [38] B.N. Taylor, C.E. Kuyatt, Guidelines for evaluating and expressing the uncertainty of nist measurement results, Natl. Inst. Stand. Technol. (US) Tech. (1993), Note 1297.
- [39] W. Sander, V.C. Willem, S. Chao, L. Detlef, On the spreading of impacting drops, J. Fluid Mech. 805 (2016) 636–655.
- [40] A.B.D. Cassie, S. Baxter, Wettability of porous surfaces, Trans. Faraday Soc. 40 (1) (1944) 546–551.
- [41] D. Bartolo, C. Josserand, D. Bonn, Retraction dynamics of aquous drops upon impact on nonwetting surfaces, J. Fluid Mech. 545 (545) (2005) 329–338.
- [42] G. Castanet, O. Caballina, F. Lemoine, Drop spreading at the impact in the leidenfrost boiling, Phys. Fluids 27 (6) (2015) 2579.
- [43] E. Villermaux, B. Bossa, Drop fragmentation on impact, J. Fluid Mech. 668 (4) (2011) 412–435.
- [44] J. Eggers, M.A. Fontelos, C. Josserand, S. Zaleski, Drop dynamics after impact on a solid wall: theory and simulations, Phys. Fluids 22 (6) (2010) 584–772.
- [45] Y. Xuan, Q. Li, Investigation on convective heat transfer and flow features of nanofluids, J. Heat Transfer 125 (1) (2003) 151–155.
- [46] V. Bahadur, L. Mishchenko, B. Hatton, J.A. Taylor, J. Aizenberg, T. Krupenkin, Predictive model for ice formation on superhydrophobic surfaces, Langmuir 27 (23) (2011) 14143.